

Functional Metal-oxide Plasmonic Metastructures: Ultrabright Semiconductor Quantum Dots with Polarized Spontaneous Emission and Suppressed Auger Recombination

Seyed M. Sadeghi,^{1,*} Waylin J. Wing,¹ Rithvik R. Gutha,¹ Ryan W. Goul,² and Judy Z. Wu²

¹*Department of Physics and Astronomy, University of Alabama in Huntsville, Huntsville, Alabama 35899, USA*

²*Department of Physics and Astronomy, University of Kansas, Lawrence, Kansas 66045, USA*



(Received 17 May 2018; revised manuscript received 27 August 2018; published 19 February 2019)

We use localized surface-plasmon resonances in metallic nanoantennas to suppress the defect environment of colloidal quantum dots and to enhance and polarize their spontaneous emission. For this we study the interaction of such quantum dots with functional metal-oxide plasmonic metastructures consisting of an Au/Si Schottky junction in close vicinity of a Si/Al oxide charge barrier. We show that optically excited quantum dots can couple with such metastructures via their electric dipole fields, offering super-plasmonic-processes that include the impact of hot electron generation and fixed negative charges at the Si/Al oxide junction. For metallic nanoantennas with small aspect ratios our results show that these metastructures can reduce the defect-induced nonradiative decay rates of quantum dots such that their lifetime can become significantly longer than those in the absence of such nanoantennas. For metallic nanoantennas with larger aspect ratios these structures lead to ultrahigh enhancement of exciton-plasmon coupling, making the spontaneous emission of quantum dots strongly polarized while increasing their emission intensities by about 50 times. These results show by keeping excitons in the cores of quantum dots, the metastructures suppress migration of photoexcited electrons to surface defects and, therefore, reduce Auger recombination. Coherent dynamics associated with the quantum-dot-induced exciton-plasmon coupling is theoretically investigated.

DOI: 10.1103/PhysRevApplied.11.024045

I. INTRODUCTION

Colloidal semiconductor quantum dots (QDs) hold the promise of many scientific and technological applications, ranging from chemical or biological sensors to photodetectors, molecular photonic nanowires, gain compensator for plasmonic metamaterials, single-photon sources, and photovoltaic systems [1–5]. One of the major obstacles that significantly hinders implementation of these applications is the presence of surface trap sites or the defect environment (DE) [3]. It is well known that fast migration of photoexcited electrons from QD cores to these sites via thermal effects [Fig. 1(a), T] or Auger processes [Fig. 1(a), 1 → 2 process], lead to many undesirable effects [3,6]. These include reduction of quantum yields of QDs, heat generation, fluorescence blinking, quantum decoherence, etc.

Another major issue that QDs are facing is their long radiative lifetimes, which is typically in the range of tens of ns. A prime impact of this feature is the fact that it can make the adverse effects of the DE even more dramatic. Basically, in typical QDs the radiative recombination

decay needs to compete with the ultrafast nonradiative processes caused by the DEs. Therefore, the spontaneous emission rate can be easily overwhelmed by the nonradiative decay rates. In this regard, in addition to structural optimization of the QDs [7,8], the ongoing research heavily relies on application of microcavities, plasmonic nanocavities, and metallic nanoantennas (mANTs) [9–17]. These techniques are mostly based on enhancement of the electric field experienced by the QDs. This process increases the rates of their spontaneous emission (Purcell effect), allowing them to compete better with the nonradiative decay processes [18–20]. In such techniques, which are referred to in the following as “normal” plasmonic, the inherent issues associated with the surface defects remain unresolved.

One of the main objectives of this paper is to show that localized surface-plasmon resonances (LSPRs) associated with mANTs can be used to not only enhance spontaneous emission rates of QDs, but also to suppress their DEs, including Auger recombination. For this we investigate an alternative material platform that combines the effects of Schottky junctions and Si/Al oxide surface charge barriers with LSPRs, offering super-plasmonic-processes that can present strong Purcell effect while quarantining excitons

*seyed.sadeghi@uah.edu

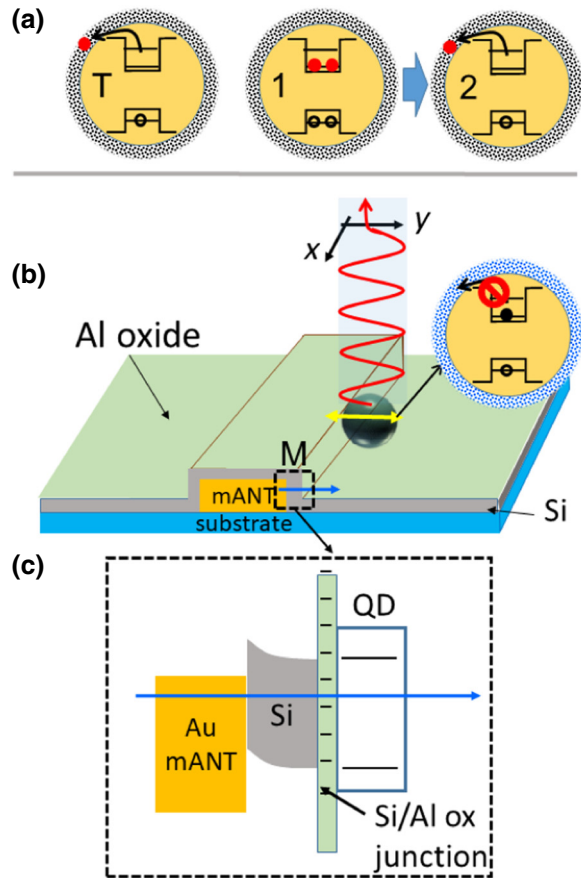


FIG. 1. (a) Schematic illustration of the migration of a photoexcited electron from QD cores to the surface defects (DE) via thermal processes (T) and Auger recombination ($1 \rightarrow 2$). (b) Polarized emission of QDs combined with suppression of the defect environment via a functional metal-oxide plasmonic metastructure. (c) Energy diagram associated with junctions between mANT/Si/Al oxide/QDs along the horizontal blue arrow highlighted in the dashed square region in (b). The hyphens in the Al oxide layer represent the fixed negative charges at the Si/Al oxide junction.

against the surface defects. The structures studied in this paper, called functional metal-oxide plasmonic metastructures (FMOP), consist of arrays of gold (Au) mANTs embedded in a Si layer and capped with an ultrathin layer of Al oxide [Fig. 1(b)]. The structural design of FMOP is such that the incident light only excites the QDs placed close to the Al oxide layer. The dipole fields of such QDs then interact with the mANTs, generating LSPRs. The plasmon fields associated with such LSPRs then interact with the same QDs, setting up exciton-plasmon coupling. We show that in the presence of the Si/Al oxide junction and the Schottky barrier formed at the Au/Si interface [Fig. 1(c)], plasmonic effects can inhibit migration of photoexcited electrons to the surface defect sites [Fig. 1(b)] while Purcell effect enhances the spontaneous emission rate of the QDs. We discuss how these are associated with

the fixed negative surface charges formed at the Si/Al junction [21], and hot electron transfer across the Schottky barrier at the Au/Si interface [22–24].

The results of this paper highlight the impact of aspect ratios of the mANTs, demonstrating that when these ratios are small FMOP can support strong lifetime elongation, indicating efficient quarantine of excitons against DEs. We demonstrate that the extent of this process is such that the lifetimes of the QDs can even become longer than those in the absence of mANTs. This shows the prime impact of hot electrons in the field passivation of DEs when such mANTs are involved. Our results show that when the mANTs have large aspect ratios, the distinct polarization dependencies of LSPRs allows FMOP to support significant enhancement of QD-induced exciton-plasmon coupling. This leads to alignment of electric dipole moments of QDs along certain directions [Fig. 1(b)], allowing their spontaneous emission to become strongly polarized while their intensities are increased by about 50 times. We theoretically study coherent and incoherent dynamics caused by such a QD-induced exciton-plasmon coupling, discussing the impact of its phase. The results of this paper offer novel enabling processes that not only can improve current applications of QDs, but also can form the key ingredients of many other applications, ranging from quantum devices and computations, sensors, optical, and opto-electronics devices [25–30].

Note that this paper is related to our recent reports, demonstrating the impact of metal-oxide plasmonic metafilms on emission QDs [31,32]. In these reports, thin films of Au combined with Si/Al oxide charge barriers were used to suppress the impact of the DEs of QDs [31]. Because of the lack of strong LSPRs in the case of Au thin films, the metafilms did not support strong exciton-plasmon coupling and DE suppression. In this paper these issues are addressed using LSPRs in mANTs.

II. METHODOLOGY

The FMOP structures studied in this paper are based on three processes. The first is generation of hot electrons and their transfer across the Schottky barrier to the Si layer in an Au/Si junction [24,33–35]. The second process is formation of fixed negative surface charges at Si/Al oxide junctions [36,37]. As a result, such junctions can lead to field passivation of QDs by suppressing transfer of their photoejected electrons to the defect sites [38–40]. The third process is excitation of LSPRs via the dipole fields of the QDs. Such QD-induced plasmons can generate a strong field back in the QDs, setting up exciton-plasmon coupling [41–43].

Considering these features, we fabricate two types of Au mANT arrays onto micro cover glass substrates using e-beam lithography. In array A each mANT has a width of approximately 130 nm and a length of approximately

220 nm, and is separated from each other by 500 nm [Fig. 2(a)]. In array B, the lengths of mANTs are 890 nm and their widths 190 nm. The lattice constants of this array along the x axis is 1000 nm and along the y axis is 500 nm [Fig. 3(b) inset]. In both arrays the heights (thickness) of mANTs are 40 nm. A 15-nm layer of Si is then sputtered on the top of these arrays [Fig. 1(b)]. The thickness of the Si layer is optimized to support “normal” plasmonic emission enhancement, i.e., enhancement of emission combined with lifetime suppression. This layer has a large number of defect sites but it can also support a band gap [44]. After this, an Al oxide layer with a nominal thickness of approximately 1 nm is sputtered on the top of the Si layer [Fig. 1(b)]. As shown in Ref. [32], such a thickness allows formation of Al oxide grains with optimized sizes that can lead to efficient FMOP. We also fabricate reference samples wherein the Si layer is replaced with a SiO_2 layer or the Al oxide layer is not present. The samples are completed after a solution of QDs in toluene is spin coated on the top of them, in contact with the Al oxide layer. The thickness of the QD films are estimated to be about 50 nm. The QDs are excited with Ar lasers with 514-nm wavelength. The emission of the QDs is collected by a set of optics and is directed towards a spectrometer. The QDs are acquired from NN-Labs, LLC. They are CdSe/ZnS nanocrystals coated with octadecylamine ligands with emission at 640 nm. To measure the decay of QDs we use a time-correlated single-photon counting (TCSPC) system (Picoquant Pico-Timeharp 260) combined with a 30-ps pulsed laser with 450-nm wavelength.

Figure 2(b) shows the AFM image of sample A after deposition of the 15 nm of Si. Compared to the top-view SEM image of this sample taken before the deposition [Fig. 2(a)], the outcomes show how the mANTs are coated with Si. This can be seen better in Fig. 2(c) where we show the surface profile along the arrow in Fig. 2(b). Based on these images we infer that the lengths and widths of the Si-coated mANTs, measured 20 nm from the top, are 280 and 206 nm. These results show that the Si layer covers the mANTs but the spacings between the mANTs remain widely open. Considering these, we believe an effective interaction between QDs with the mANTs happens as schematically shown in Fig. 1(b). This figure shows the projection of the QDs’ dipoles along the y axis. These dipoles are formed after formation of excitons. As discussed in the following, the configuration shown in Fig. 1(b) plays a crucial role in the generation of hot electrons that is responsible for suppression of DEs of the QDs. A similar situation as that in Fig. 2(b) is also observed for array B. Figure 3(b) inset shows the top-view SEM image of this sample before the Si layer is added.

Figure 3 shows the extinction spectra of arrays A (a) and B (b) after deposition of the Si layer when the incident light was normal to the planes of the arrays and its

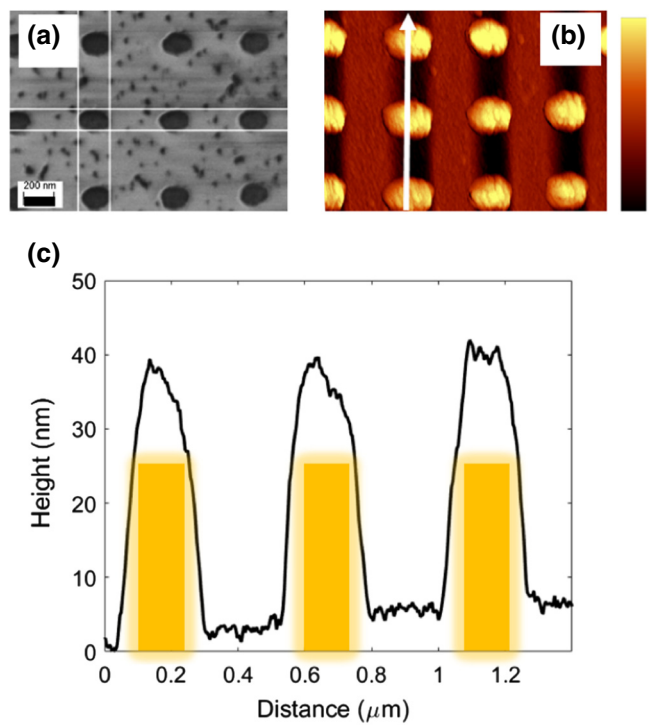


FIG. 2. (a) SEM image of array A containing mANTs with $L = 200$ nm and $W = 135$ nm, (b) its AFM image profile after deposition of 15 nm of Si, and (c) variation of height along the arrow shown in (b). The color-coded bar in (b) shows the range of height from 0 to 33 nm. The scale bar in (a) is 200 nm.

polarization is either along the y or x axis [Fig. 3(b) inset]. Along the x axis, the spectrum of array A shows two LSPR responses of the mANTs (dashed line), one at approximately 600 nm (peak A) and the other at approximately 1062 nm (peak B). Along the y axis (solid line) we can see a LSPR peak at about 612 nm (peak C) and a sharp peak associated with the surface lattice resonance (SLR) of the mANT array at about 796 nm (peak D). This mode is formed by the hybridization of LSPRs in the superstrate with Rayleigh anomaly [45–48]. The QD emission occurs around the LSPR (dashed arrow) at approximately 640 nm and is not affected by the SLR.

The extinction spectra of array B are shown in Fig. 3(b). Along the y axis (solid line) we see two main features, one at about 620 nm (peak L) and the other at 760 nm (peak M). The latter is associated with SLR, as the case of peak D in array A. The reason that the wavelengths of peaks M and D are close to each other is related to the fact that both arrays have the same lattice constants along the y axis (500 nm). The small difference in the wavelengths of these two peaks (approximately 36 nm) is due to dependency of SLR on the specifications of mANTs, including detuning of their LSPRs (peaks L and C) from Rayleigh anomaly. Along the x axis, however, since the lengths of mANTs in array B are rather long, its extinction mostly refers to the multipolar

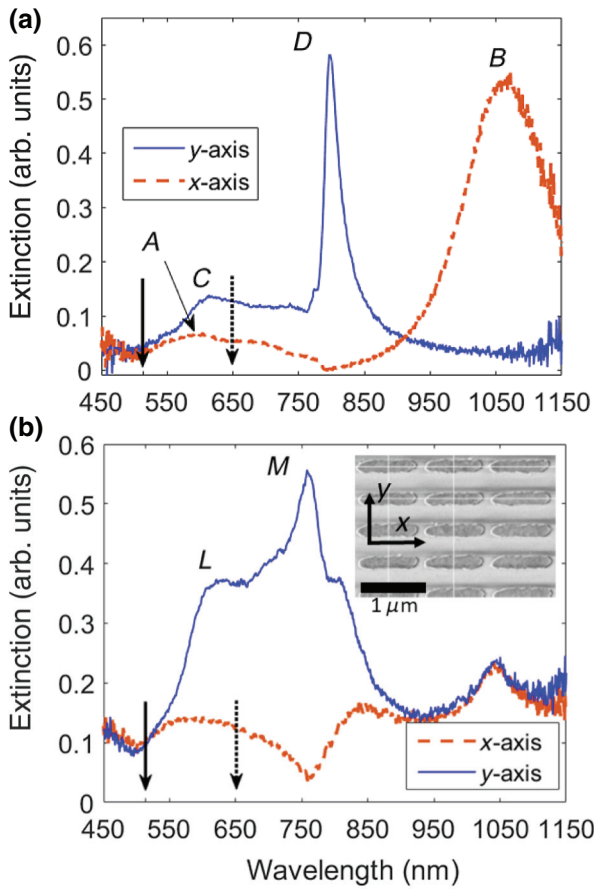


FIG. 3. Extinction spectra of arrays A (a) and B (b) coated with 15 nm of Si. The vertical solid and dashed arrows locate the wavelengths of the laser (514 nm) and QD peak emission (640 nm), respectively. The solid and dashed lines in (a) and (b) refer to the cases when the incident light is polarized along the *y* and *x* axes (legends). The inset in (b) shows the top-view SEM image of array B before adding Si.

nature of the longitudinal LSPRs [49–51]. This includes the peak seen at about 1045 nm, which based on Ref. [51], can be due to third multipole resonance. Note that in both cases the dashed and solid line arrows refer to the wavelengths of the emission of QDs and excitation laser (514 nm), respectively. Additionally, the spectral overlap for *x* and *y* axes for wavelength longer than 850 nm in Fig. 3(b) is caused by the polarizer cutoff.

III. MATERIAL ENVIRONMENT FOR SUPPRESSION OF THE DEFECT ENVIRONMENT

We start our investigation by considering the emission intensity and dynamics of QDs in the presence of array A but in the absence of Al oxide junction (mANT/Si system). Under this condition, the Si/Al oxide junction does not exist and “normal” plasmonics should occur. As shown in Fig. 4(a), under these conditions the emission intensity of the QDs on mANT/Si (dashed line) is about 2.4 times

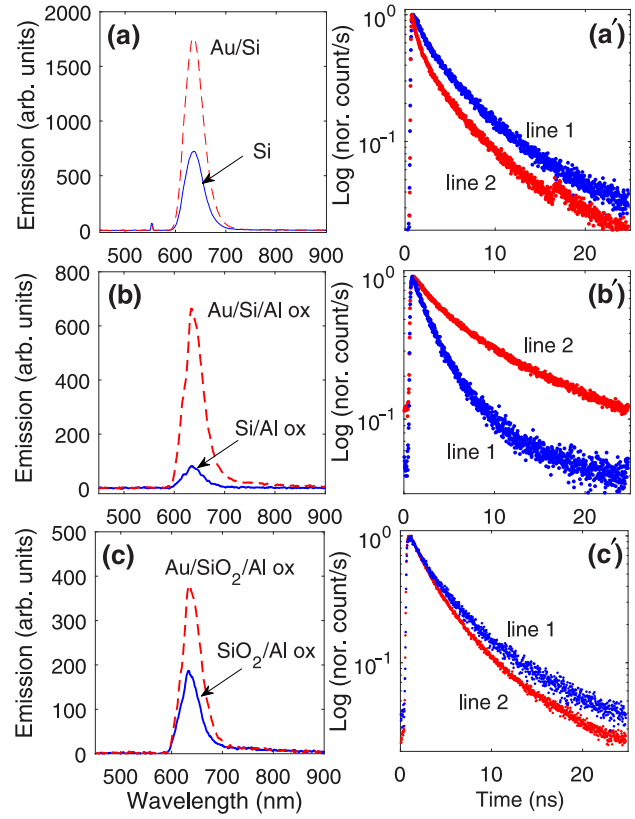


FIG. 4. Emission of QDs on Au/Si and Si (a), Au/Si/Al oxide and Si/Al oxide (b) and Au/SiO₂/Al oxide and SiO₂/Al oxide (c). (a')–(c') refer to their corresponding decay in logarithmic scale, wherein lines 1 and 2 present the cases in the absence and presence of Au mANTs (nor. count/s refers to the normalized count per second). In (a)–(c) solid lines refer to the emission in the absence of mANTs and the dashed line to those in the presence of the mANTs.

larger than those on Si, i.e., in the absence of mANTs (solid line). Figure 4(a') shows the decay of emission of the QDs for these two cases in logarithmic scale. The results show that QDs on mANT/Si (line 2) decay faster than those in the absence of the mANTs (line 1). This illustrates typical emission enhancement under “normal” plasmonics, which happens with the increase of QD decay rate [15,52,53]. The emission enhancement here is the result of the balance between reduction of spontaneous lifetime of QDs via plasmonic field enhancement (Purcell effect) and energy transfer from QDs to mANTs, which acts as a nonradiative decay channel.

To investigate this further, note that the recombination dynamics of the QDs seen in Fig. 4 follow a biexponential distribution [20,54–58]

$$I(t) = A_f e^{-t/\tau_f} + A_s e^{-t/\tau_s}. \quad (1)$$

Here A_f and τ_f refer to the amplitude and decay time of the fast process and A_s and τ_s to those of the slow

process. Such a distribution is related to fact that the surfaces of colloidal QDs play important roles in the carrier relaxation and recombination processes [59]. Therefore, electron dynamics is controlled by the surface specifications, compared to surface-independent hole relaxation. In general, the fast process is associated with trap and defect sites while the slow process is related to the interband intrinsic decay of the QDs [60].

Our fits to the decay seen in Fig. 4(a') suggest that in the absence of mANTs, i.e., in the Si/QD system, $\tau_f \sim 2.05$ ns and $\tau_s \sim 8.6$ ns. The ratio of fast to slow amplitudes (A_f/A_s) is about 1.52, suggesting that the fast process is more dominant. The results of fitting for the case of mANT/Si/QD suggest $\tau_f \sim 1.23$ ns and $\tau_s \sim 7.14$ ns, indicating about approximately 40% and approximately 17% reduction, respectively. A_f/A_s , however, increases slightly reaching approximately 1.6. These are consistent with the previous reports that showed when QDs are in the vicinity of mANTs, the relative amplitudes of their fast decay increase while τ_f becomes shorter via energy transfer to mANTs [53]. Reduction of the τ_s is due to enhancement of radiative decay rates of QDs via plasmonic field enhancement (Purcell effect) [9,52,56].

Emission of QDs on FMOP, however, offers a dramatically different picture. To see this we consider a similar structure as that used for Fig. 4(a), but before the QDs are dispersed, 1 nm of Al oxide is deposited on the top of the Si layer [Fig. 1(b)]. Figure 4(b) indicates that, compared to the case of QDs on Si/Al oxide [Fig. 4(a)], the emission intensity of the QDs on FMOP increases by about 8.2 times, offering an emission enhancement factor far more than that seen in the absence of Al oxide. But more surprising is the impact of Al oxide on the emission dynamics of the QDs. As Fig. 4(b') shows in logarithmic scale, the decay rate of QDs in the absence of mANTs (line 1) is now much larger than those in the presence of mANTs (line 2). In other words, in contrast to the common understanding, in the presence of Si/Al oxide, introduction of mANTs (formation of FMOP) not only makes the QDs much more efficient emitters, but also increases their lifetimes.

To see this better, we carry out biexponential fittings to the results shown in Fig. 4(b'). In the absence of mANTs, i.e., in the Si/Al oxide system, we found $\tau_f \sim 2.27$ ns, $\tau_s \sim 18.5$ ns, and $A_f/A_s \sim 6$, indicating the dominance of the fast process. In the case of the mANT/Si/Al oxide system (FMOP), however, τ_f and τ_s become 3.33 and 16.4 ns, respectively. This suggests the lifetime of the fast process is in fact increased while the slow process becomes more efficient. The latter is an indication of Purcell effect, which happens similarly in the case of “normal” plasmonics [Fig. 4(a')]. Increase of τ_f by about 30%, however, is a crucial feature that highlights the unique impact of FMOP on the dynamics of excitons. This process occurs along the striking results that show A_f/A_s is reduced from 6 to about 1. Combination of these processes suggests that

introduction of mANTs leads to significant reduction in the number of traps and defect sites available to excitons in QDs.

IV. ULTRAHIGH ENHANCEMENT OF EXCITON-PLASMON COUPLING

The results presented in the preceding section showed that FMOP with array A can support strong enhancement of emission of QDs and significant elongation of their lifetimes. Despite this, our polarization analysis indicated that the emission of such QDs was mostly unpolarized (not shown). This can be associated with the aspect ratios of the mANTs, which in the case of array A, were not large. One expects by varying the sizes and shapes of the mANTs this changes significantly [41,42]. To see this and, in particular, strong enhancement of exciton-plasmon coupling, in this section we consider a similar FMOP design as that in the preceding section, but use array B. As shown in Fig. 3(b), at the wavelength of the QD emission (dashed arrow), this array exhibits a strong polarization-dependent extinction. As a result, the QD-induced exciton-plasmon coupling should also become polarization dependent. Figure 3(b) suggests that for the case of array B such a coupling should be stronger along the y axis. Therefore, the projection of the QDs’ electric dipoles along the y axis should more efficiently excite plasmons and induce exciton-plasmon coupling [Fig. 1(b)] than those along the x axis. This, in turn, polarizes spontaneous emission of the QDs, which in the absence of mANTs is nearly perfectly unpolarized.

To study the emission enhancement for different states of polarization of the QDs, we put a polarization analyzer before the collective lens of the spectrometer. We collect the emission of QDs as the angle of the axis of the analyzer (θ) is changed from 0° to 180° . For $\theta = 0^\circ$ this axis is along the x axis and for $\theta = 90^\circ$ it is along y axis, i.e., long and short axes of the mANTs [Fig. 3(b) inset]. Figures 5(a) and 5(b) show the results of measurements for the emission enhancement factors for the cases of Au/Si/Al oxide (ξ_{FMOP}) and Au/Si (ξ_{norm}). ξ_{FMOP} refers to the ratio of the emission of QDs in the presence of Au/Si/Al oxide to that on Si/Al oxide. ξ_{norm} , on the other hand, is the ratio of emission of QDs on Au/Si to that on Si. Here can see ξ_{FMOP} becomes about 50 when $\theta = 90^\circ$. For $\theta = 0^\circ$ or 180° the value of ξ_{FMOP} is approximately 26 [Fig. 5(a)]. In the absence of Al oxide [Fig. 5(b)], however, ξ_{norm} is about 5.5 for $\theta = 0^\circ$ and 7 for $\theta = 90^\circ$, suggesting a much weaker polarization dependency. The results in the case of Au/Si [Fig. 5(b)] suggest QD-induced exciton-plasmon coupling as expected from “normal” plasmonics [43]. In the case of Au/Si/Al oxide [Fig. 5(a)], however, such a process is significantly more pronounced. This indicates enhancement of exciton-plasmon coupling via FMOP. Note that as shown in the inset of Fig. 5(a), the ultrahigh enhancement of exciton-plasmon coupling occurs in the presence

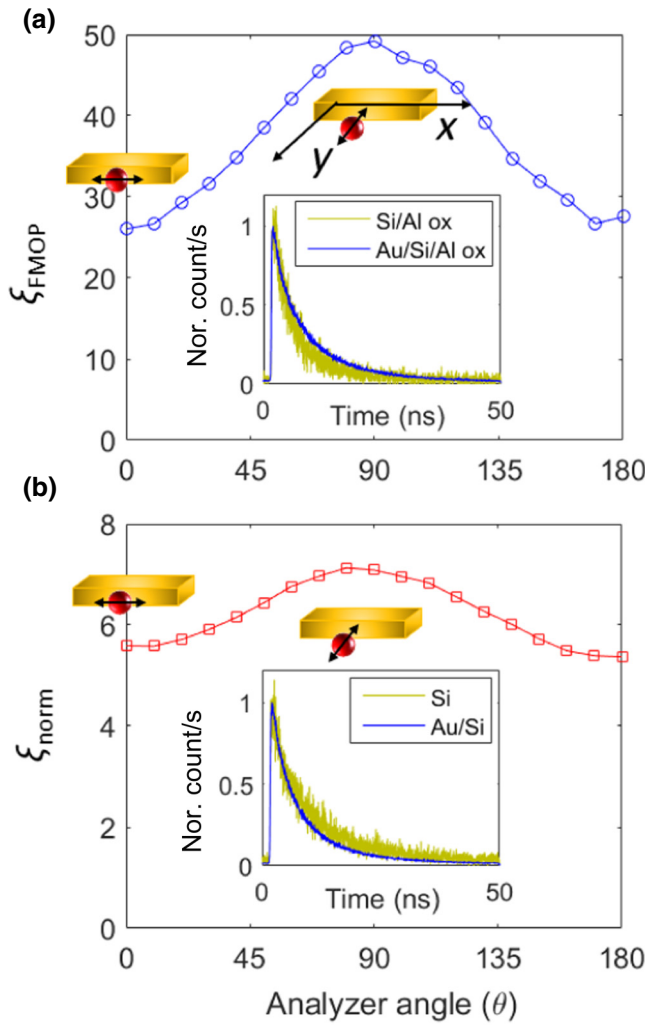


FIG. 5. Variation of emission enhancement factors of QDs on Au/Si/Al oxide (a) and on Au/Si (b). Insets show the decay rates associated with these cases and for the cases of QDs on Si/Al oxide (a) and Si (b). The schematics at $\theta = 0^\circ$ and 90° show the prominent directions of the QD dipoles with respect to the mANTs.

of lifetime elongation of QDs, although to a lesser degree compared to what happened in the case of Fig. 4(b'). In the case of Au/Si, we see normal plasmonics [Fig. 5(b) inset]. The schematics seen at $\theta = 0^\circ$ and 90° in Fig. 5 show the effective projection of the QD dipoles with respect to the mANTs for these angles.

To investigate this further in Fig. 6 we show the polar plots of the emission enhancement factors of QDs on glass, Au/Si/Al oxide (ξ_{FMOP}), and Au/Si (ξ_{norm}) as a function of θ . Here we also consider the impact of the polarization of the excitation laser beam. In Fig. 6(b) we consider this laser is polarized along the y axis (y-pol excitation) and in Fig. 6(c) this laser is polarized along the x axis (x-pol excitation), as in the case of Fig. 5. The results in Fig. 6(a) basically highlight that the emission of QDs on glass is

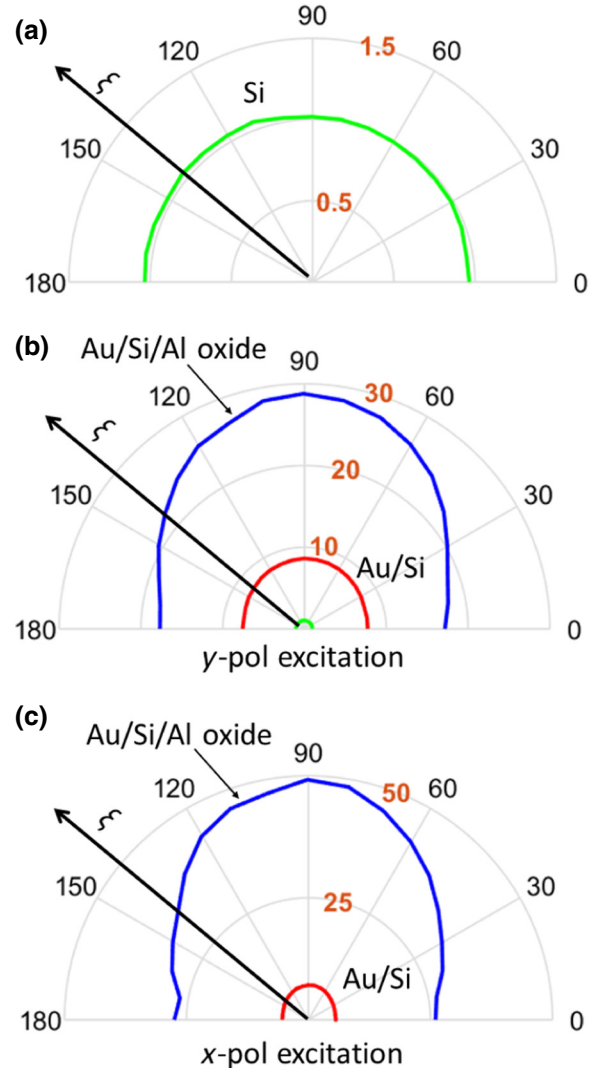


FIG. 6. Polar plots of emission enhancement factors (ξ) of QDs on glass (a), and on Au/Si/Al oxide (ξ_{FMOP}) and Au/Si (ξ_{norm}) when the incident laser beam is polarized along the y pol (b) and along x pol (c) as a function of θ .

unpolarized. In the case of the y -pol excitation, the emission enhancement reaches about 28 when $\theta = 90^\circ$ and 18 when $\theta = 0^\circ$ [Fig. 6(b)]. Variations of enhancement factor with θ and its values for the case of Au/Si (ξ_{norm}) are much smaller.

For the case of the x -pol excitation [Fig. 6(c)], however, we observe the amount of emission enhancement increases drastically, reaching about 50 for $\theta = 90^\circ$ and 25 for $\theta = 0^\circ$. In this paper, however, as mentioned before, plasmons are mostly excited by the QDs, not direct excitation with the laser field. In fact, as can be seen in Fig. 3(b), array B shows very small but similar extinctions for the x pol and y pol around the laser wavelength (514 nm). Considering these, we associate the difference between the x -pol and y -pol excitations in Figs. 6(b) and 6(c) to the difference

between the optical modes supported by this array for such excitation schemes. In fact, for a typical length of mANTs as in array B, for x pol the optical modes can be concentrated more on the top of the array[61]. This enhances the optical excitation of the QDs, leading to higher emission enhancement.

V. KEEPING EXCITONS IN THE QUANTUM-DOT CORES USING LSPRS

The results shown in the preceding sections highlight the crucial impact of the Si/Al oxide junction on the dynamics of QDs and, in particular, increase of their lifetime. To highlight the effects of such a junction further, we replaced the Si layer with a SiO_2 layer with the same thickness (15 nm) while keeping mANT arrays very similar to those used in Figs. 4(b) and 4(b'), forming a mANT/ SiO_2 /Al oxide structure. In other words, we replaced Si/Al oxide charge barrier with a SiO_2 /Al oxide junction. The results seen in Fig. 4(c) indicate that the amount of emission enhancement becomes very modest (2.1 times), similar to that seen in Fig. 4(a). This happens, as the dynamics of the QD emission also become normal, i.e., QDs decay faster on mANTs than in their absence, as seen in Fig. 4(c') (lines 1 and 2, respectively). Fitting the data presented in Fig. 4(c') also shows that in the absence of mANTs $\tau_f \sim 2.66$ ns, $\tau_s \sim 11.1$ ns, and $A_f/A_s = 2.24$. In the presence of mANTs we obtained $\tau_f \sim 2.36$ ns, $\tau_s \sim 9.52$ ns, and $A_f/A_s \sim 3$. These results show a similar trend as those seen in the case of mANT/Si [Fig. 4(a')], highlighting the unique role played by the Si/Al oxide junctions in the dynamics of QDs in the presence of FMOP [Fig. 4(b')].

The results presented in Fig. 4 show that the Si/Al oxide junction plays a key role in the lifetime elongation combined with Purcell effects. This issue and the impact of structural parameters of such a junction have been discussed by us in Refs. [31,32]. A distinct difference between the results in this paper and those obtained in these references, is the fact that here we are dealing with mANT arrays, rather than thin Au films with rough surfaces. As shown in Fig. 3 these arrays support strong polarization-dependent LSPRs. Inspection of this figure shows that around the wavelength of the excitation laser (514 nm) the mANT arrays are nearly transparent. Therefore, this laser predominantly excites QDs off resonantly. As schematically shown in Fig. 7(a), following their fast relaxation, the photoexcited electrons and holes form near-band edge excitons. The dipole fields of such excitons then excite plasmons, forming QD-induced exciton-plasmon coupling [42,43].

Considering this, to discuss the results presented in this paper let us start with “normal” plasmonic, i.e., no Si/Al oxide charge barrier. In this case, as schematically shown in Fig. 7(b), the photoexcited electrons in QDs can migrate to the defect sites at the surface of the QDs and inside the

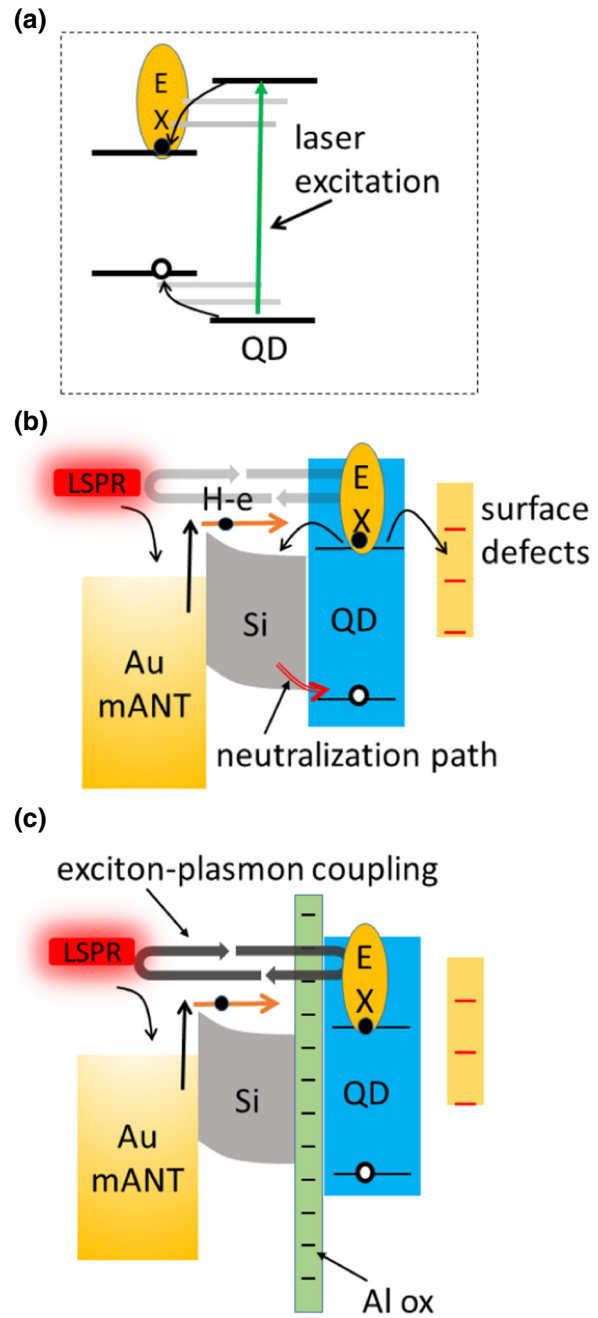


FIG. 7. Schematics of the off-resonant optical excitation of QDs and electron or hole relaxation (a) and energy band diagrams and hot electron transfer in Au/Si/QD (b) and Au/Si/Al oxide/QD systems (c). In (a) the green vertical arrow represents the off-resonant excitation of the QDs. HE refers to the hot electrons.

amorphous Si layer. At the same time, LSPRs can decay delivering their energies to electrons in the mANTs, forming hot electrons (HE) [23,62]. In the absence of the Si/Al oxide charge barrier, the neutralization path of the QDs are open, allowing hot electrons (HE) in the Si layer to reach the QDs. In addition to these, such a system supports

an energy transfer channel from the QDs to mANTs via Forster resonance energy transfer (FRET). This mechanism is not involved with exchange of electrons or holes. To avoid complication in the illustration, this mechanism is not highlighted in Fig. 7(b). Additionally, note that plasmonic effects under these conditions do not influence the rates of the photoexcited electrons' transfer from QDs to the Si layer or DE.

Adding the Si/Al oxide charge barrier (FMOP) changes this picture significantly. The mechanisms behind the results of FMOP can include (i) exciton-plasmon coupling, and (ii) field-effect passivation of the DEs of QDs via Al oxide charge barrier and electrostatic charging of the Si layer by hot electrons [Fig. 7(c)]. The key effects of the Si/Al oxide charge barrier are blocking the neutralization path and formation of an electrostatic field that pushes the photoexcited electrons back to the QDs, i.e., keep them in their cores. On the other hand, the geometrical specifications of mANTs of our samples, array A in particular, can support an efficient transfer of hot electrons from mANTs to the Si layer. This can be related to the recent studies that showed hot electrons are more efficiently excited along the same direction at the polarization of the incident light [23,62], and when mANTs are embedded in a semiconductor [63]. In the structures considered in this paper the mANTs are embedded in Si [Fig. 2(b)] and LSPRs are excited by the QD dipoles. Therefore, we expect efficient transfer of hot electrons along the direction of dipole moments of QDs from mANTs to the Si layer across the Schottky barrier. In the presence of the Si/Al oxide charge barrier since the neutralization path is blocked, hot electrons have a higher chance to accumulate in the Si layer. This forms an electrostatic field similar to that of the Si/Al oxide charge barrier, leading to a stronger confinement of the photoexcited electrons in the QDs' cores.

The hot electron generation in the case of array A can be more efficient than array B. This is because of the fact that, since the aspect ratio of mANTs in array A is not large, the QD dipoles can excite mANTs along both x and y axes. This explains why the lifetime elongation in the case of this array is more efficient than array B. A good indicator of efficient field passivation for the case of this array can be seen in Fig. 4(b'), wherein the results show that when mANTs were introduced to Si/Al oxide, A_f/A_s is reduced from approximately 6 to approximately 1. For the case of array B when the QD dipoles are along the y axis the coupling between the excitons and plasmons is stronger. In fact, comparison between the results in Figs. 5(a) and 5(b) shows that this process (or exciton-plasmon coupling) significantly enhances because of the contribution of the hot electrons and Si/Al oxide charge barrier.

Note that Auger processes can become significant when the QDs become charged. As depicted in Fig. 1(a) (processes 1 to 2), this can happen when photoexcited electrons (or holes) of QDs migrate to the DE [3]. Considering this,

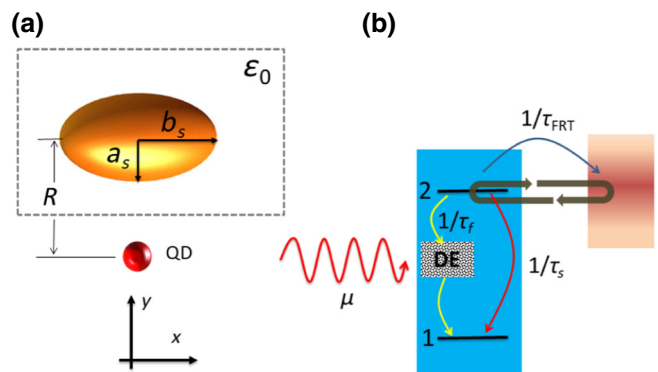


FIG. 8. Schematics of the single QD-mANT system (a) and its electronic transitions (b) used in the theoretical model. Here R refers to the center-to-center distance between the QD and the mANT. μ highlights the prime purpose the laser field to excite the dipole moments of the QD.

suppression of DE and electron migration to the surface defects, as discussed above, can lead to a smaller chance of Auger recombination. This can, at least, partially be responsible for the large enhancement of emission of QDs in Au/Si/Al oxide systems seen in Figs. 4(b) and 5(a).

VI. COHERENT DYNAMICS OF QD-INDUCED EXCITON-PLASMON COUPLING

As highlighted in the preceding section the plasmons discussed in this paper are not generated directly by the laser field, but rather via the dipole fields of the QDs. The off-resonant excitation of QDs [Fig. 7(a)] can lead, in general, to excitons with random phases and electric dipole moment directions. Figure 5(a), however, suggests that a large number of these dipoles are engaged efficiently with the transverse modes of mANTs, highlighting their preference for being aligned along the y axis. Since the QD-induced plasmons can be in phase with the excitons that drive them, an interesting question is the degree of quantum-coherence effects in our QD-mANT systems. To discuss this issue and the QD-induced exciton-plasmon coupling, in this section we present a model that can provide some insight into the coherent and incoherent dynamics in such systems. This model includes a system, a Au mANT, and a QD with a center-to-center distance of R [Fig. 8(a)]. We consider the mANT is embedded in a material (matrix) with the dielectric constant $\epsilon_{0m} = 11.56$ (as Si) and the environment of the QD has a dielectric constant of $\epsilon_{0q} = 1$ (air). The dielectric constants of the QD and mANT are represented by ϵ_s and $\epsilon_m(\omega)$, respectively. Here $\epsilon_m(\omega) = \epsilon_{IB}(\omega) + \epsilon_D(\omega)$, which is a combination of the contribution of d electrons [$\epsilon_{IB}(\omega)$] and s electrons [$\epsilon_D(\omega)$]. We also approximate the mANT with a prolate spheroid with diameters of a_s and b_s [Fig. 8(a)].

Here we are mostly interested in two cases wherein the QD dipoles are either along the x or y axis. We consider

the QD-mANT system interacts with a pulsed laser field [$E_1 = E_0^{(1)}(t) \cos(\omega_1 t)$] with a frequency (ω_1). This laser is assumed to be resonant with the QD fundamental exciton transition, which is referred to as the 1–2 transition [Fig. 8(b)]. Therefore, it acts as a driver for generation of QD dipoles with certain orientations. To make sure that this is consistent with the experimental condition wherein QDs were off-resonantly excited, we assume the intensity of this laser to be so small that it supports very small Rabi frequency, much smaller than the depolarization rate of the excitons. A key feature of our model, however, is that this laser does not excite plasmons directly, rather they are generated by the QD dipoles [Fig. 8(b)]. Considering these conditions, the total field experienced by the QD can be written as follows [30,64]:

$$E_{\text{QD}} = \frac{E_0^1(t)}{2\varepsilon_{0q}} + \frac{\beta^2 \gamma a_s b_s^2}{\varepsilon_{0q} \varepsilon_{\text{effl}}} \frac{\mu_{12} \rho_{21}}{R^6}. \quad (2)$$

Here the first term is the visible laser field and the second term is the self-induced field caused by the QD via the mANT (plasmons). In this equation $\varepsilon_{\text{effl}} = (2\varepsilon_{0q} + \varepsilon_s)/3\varepsilon_{0q}$ and μ_{12} is the dipole moment associated with the 1–2 transition considered to be $0.65 \text{ e} \times \text{nm}$ [64]. Additionally, $\beta = 2$ when the laser field is polarized along the y axis and -1 when it is polarized along the x axis [Fig. 3(a)]. γ in Eq. (2) is the polarization of the spheroid given by

$$\gamma = \frac{[\varepsilon_m(\omega) - \varepsilon_{0m}]}{[3\varepsilon_0 + 3\kappa [\varepsilon_m(\omega) - \varepsilon_{0m}]} \cdot \quad (3)$$

Here κ is the depolarization factor of the spheroid when the incident electric field of the laser is polarized along a_s [30].

ρ_{21} in Eq. (2) relates to quantum coherence in the QD. To obtain this we need to solve the equation of motion for the density matrix of the QD, ρ [65]:

$$\frac{d\rho}{dt} = -\frac{i}{\hbar}[H_{\leftrightarrow}(\rho), \rho(t)] + [\mathcal{L}\rho]_{\text{damp}}. \quad (4)$$

Here $[\mathcal{L}\rho]_{\text{damp}}$ refers to the damping terms and $H_{\leftrightarrow}(\rho)$ is the Hamiltonian of the QD wherein “ \leftrightarrow ” refers to its self-normalization process caused by its dependency on ρ . $H_{\leftrightarrow}(\rho)$ is given as [66]:

$$H_{\leftrightarrow}(\rho) = \sum_{j=1,2} \hbar\omega_j \sigma_{jj} + \hbar[\Omega_{12}^r(\rho)\sigma_{21}] + \text{H.c.}, \quad (5)$$

where $\sigma_{ij} = |i\rangle \langle j|$, $\hbar\omega_j$ represents the energy of $|j\rangle$. Ω_{12}^r is the normalized Rabi frequency of the QD, defined as

$$\Omega_{12}^r(\rho) = \Omega_{12}^0 + \eta_{\text{NR}} \rho_{21}. \quad (6)$$

Here $\Omega_{12}^0 = \mu_{12} E_0^{(1)}/2\hbar\varepsilon_{\text{effl}}$ is referring to the Rabi frequency of the QD in the absence of the mANT and $\eta_{\text{NR}} =$

$\beta^2 \gamma \mu_{12} a_s b_s^2 / (\pi \hbar \varepsilon_{0q} \varepsilon_{\text{effl}}^2 R^6)$. As mentioned above, compared to the overall dephasing rate of the system, Ω_{12}^0 is considered to be very small.

Considering these, the diagonal terms of the density-matrix elements of the QD are found as [64,67]:

$$\dot{\rho}_{11} = -2\text{Im}[\Omega_{12}^0 \rho_{21}] + 2 \frac{|\rho_{21}|^2}{\tau_{\text{FRT}}} + \Gamma_{21} \rho_{22} - \Gamma_{11} \rho_{11}, \quad (7)$$

$$\dot{\rho}_{22} = 2\text{Im}[\Omega_{12}^0 \rho_{21}] - 2 \frac{|\rho_{21}|^2}{\tau_{\text{FRT}}} - \Gamma_{21} \rho_{22}, \quad (8)$$

and

$$\dot{\rho}_{21} = -[i\hbar\Delta_{12} + \text{Re}[\eta_{\text{NR}}]\delta] + \gamma_t \rho_{21} - i\Omega_{12}^0 \delta. \quad (9)$$

Here $1/\tau_{\text{FRT}} = \text{Im}[\eta_{\text{NR}}]$ is the rate of Forster resonant energy transfer (FRET) from the QD to the mANT in the absence of quantum coherence [68]. Also $\delta = \rho_{11} - \rho_{22}$, $\Delta_{12} = \omega_{21} - \omega_1$ where ω_{21} is the frequency associated with the 1–2 transition. We consider the wavelength of this transition to be 625 nm (dotted-dashed line in Fig. 9) and $\Delta_{12} = 0$. $\Gamma_{21} = 1/\tau_s + 1/\tau_f$ in Eqs. (7) and (8) refers to the energy relaxation rate of the QD via radiative (slow process) and DE (fast process). γ_t in Eq. (9) is the total polarization dephasing rate of the QD given by

$$\gamma_t = \frac{\Gamma_{21}}{2} + \gamma_{\text{FRT}}^{\text{nor}} + \gamma_{\text{dep}}^{\text{pure}}. \quad (10)$$

Here $\gamma_{\text{FRT}}^{\text{nor}} = (1/\tau_{\text{FRT}})\delta$ is the normalized FRET rate contributing to the dephasing of the QD and $\gamma_{\text{dep}}^{\text{pure}}$ refers to the pure depolarization rate of the excitons caused by their

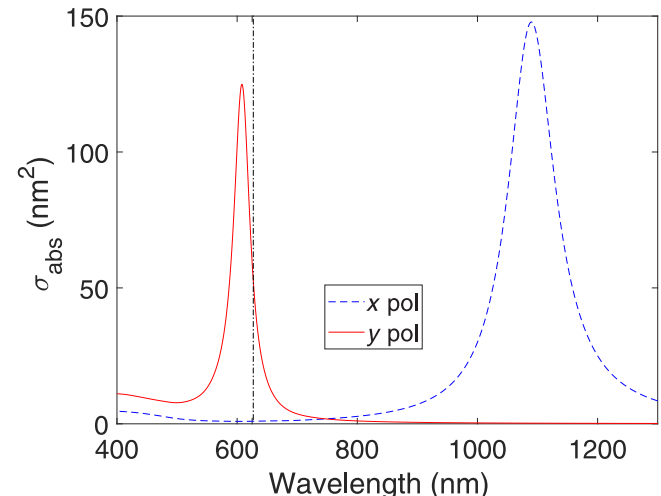


FIG. 9. Absorption cross section of the Au spheroid when the incident light is polarized along the y axis (solid line) and x axis (dashed line). Here $a_s = 4$ and $b_s = 8 \text{ nm}$ and the spheroid is imbedded in Si. The vertical dashed-dotted line refers to the wavelength of the QD transition, i.e., the 1–2 transition in Fig. 8.

elastic scattering with DE, phonons, etc. At room temperature $\gamma_{\text{dep}}^{\text{pure}} \sim 2 \text{ ps}^{-1}$ [66]. Γ_{11} refer to the decay of the ground state, which is considered to be zero.

To implement this model, we consider a Au spheroid with $a_s = 4$ and $b_s = 8 \text{ nm}$. Figure 9 shows the absorption cross section of such a spheroid when the incident light is polarized along the y axis (solid line) and x axis (dashed line). These peaks are similar to peaks C and B for array A in Fig. 3(a). Here, however, we do not see any sign of peak D , since our model only includes a single mANT.

We consider the pulsed laser field has a temporal width of approximately 150 ps and its peak intensity is 20 kW/cm² (Fig. 10, inset). This leads to $\Omega_{12}^0 = 25 \text{ ns}^{-1}$, which is significantly smaller than the pure dephasing time of the QD (2 ps⁻¹). This pulse interacts with the QD-mANT system at 10 ns of the scale shown in Fig. 10. Noting that the emission intensity of the QD can be obtained using $I(t) \propto \rho_{22}(t)$, we solved Eqs. (7)–(9) for slow and fast processes described in Sec. III. The total intensity is then obtained by considering

$$I_t(t) \propto A_f \rho_{22}^f(t) + A_s \rho_{22}^s(t), \quad (11)$$

wherein ρ_{22}^f and ρ_{22}^s are solutions of Eq. (4) for the slow and fast processes. Considering the energy relaxation rates and amplitudes obtained for each process for Si/Al oxide and Au/Si/Al oxide (FMOP) systems in Sec. III, we study the way emission of the QD, based on our model, is

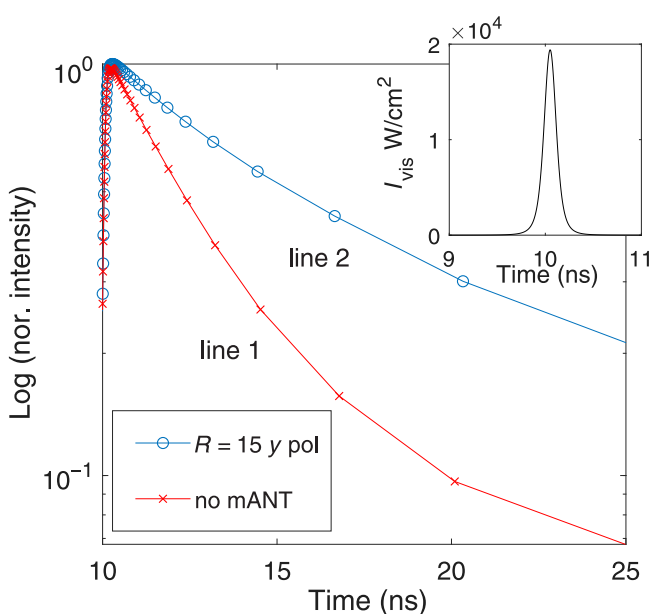


FIG. 10. Decay of normalized emission intensity of the QD in logarithmic scale when $R = 15 \text{ nm}$ (line 2) and $R = 1500 \text{ nm}$, i.e., no mANT effect (line 1). The incident light is considered to be polarized along the y axis and has the intensity and temporal profile as shown in the inset.

changed with time. Figure 10 presents the results corresponding to Si/Al oxide (line 1) and Au/Si/Al oxide (line 2) in logarithmic scale. For the latter, R is assumed to be 15 nm for the former R is considered to be so large such that the impact of mANT can be ignored. These results match fairly well with those in Fig. 4(b'). This is not unexpected, since after the incident laser pulse, the system can be described well by a rate equation for ρ_{22} .

Note that the signatures of the QD-induced exciton-plasmon coupling should happen during the temporal width of the incident laser pulse (approximately 150 ps). To see this in Fig. 11(a) we present the outcomes of the model for ρ_{21} when $R = 10 \text{ nm}$ and the incident light is polarized along the y axis (y pol). The results show that during the pulse the real (solid line) and imaginary (dashed line) parts of ρ_{21} are comparable. When the incident light becomes polarized along the x axis (x pol), as Fig. 11(a') shows, the imaginary part increases while the real part is suppressed significantly. Since ρ_{21} is an indicator of quantum coherence, this suggests that how a single QD can strongly drive the plasmons. For x pol, however, the value of the imaginary part of ρ_{21} is just an indication of the absorption of the QD.

An interesting feature regarding the QD-induced excitation-plasmon coupling is the way it influences energy transfer from the QD to the mANT. A key observation in Eqs. (7)–(9) is that depolarization rate of the QD has become dependent on the exciton density via $\Gamma_{\text{FRT}}^{\text{nor}}$

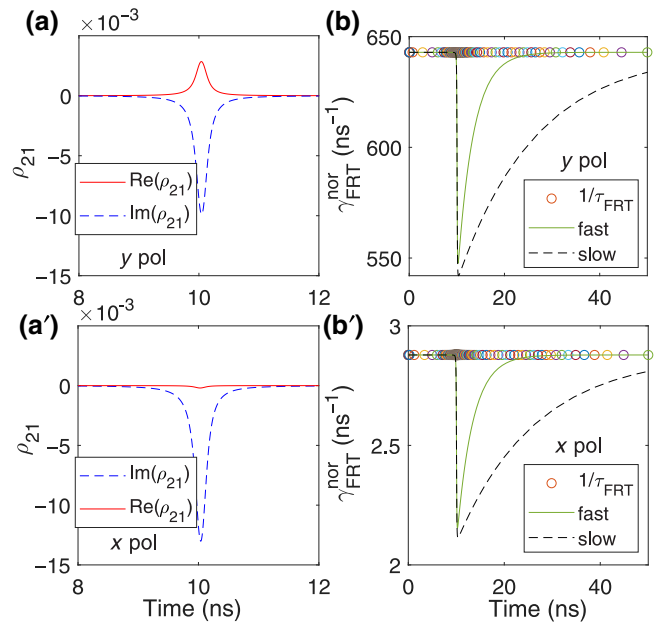


FIG. 11. Real (solid line) and imaginary (dashed line) part of ρ_{21} when the incident light is polarized along the y axis (a) and x axis (a'). (b) and (b') show $\frac{1}{\tau_{\text{FRT}}}$ (circles) and normalized FRET rate ($\gamma_{\text{FRT}}^{\text{nor}}$) for both fast (solid line) and slow (dashed line) processes.

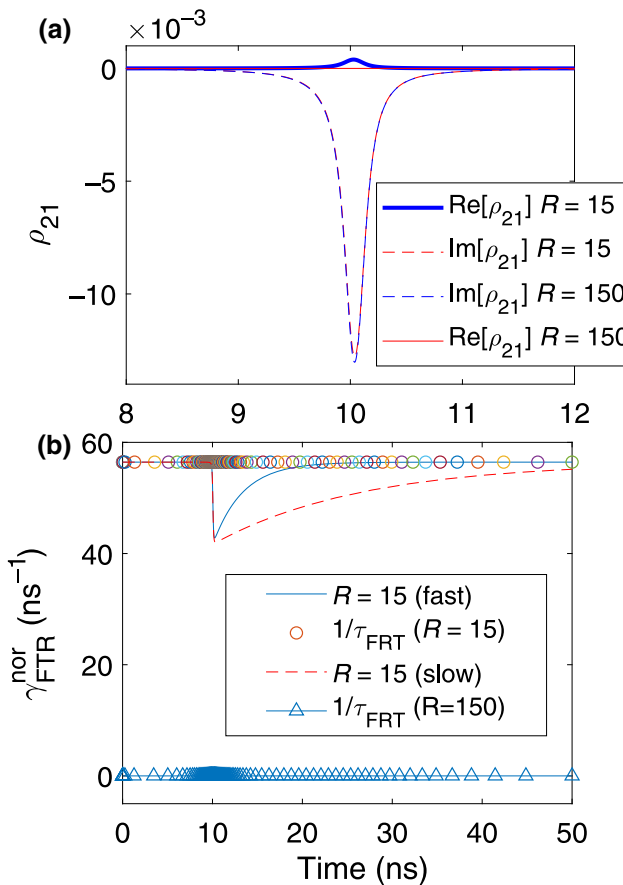


FIG. 12. (a) Real (solid lines) and imaginary (dashed lines) parts of ρ_{21} for $R = 15$ and 150 nm. (b) The corresponding $\gamma_{\text{FRT}}^{\text{nor}}$ and $1/\tau_{\text{FRT}}$ associated with these distances.

[Eq. (10)]. To see this in Figs. 11(b) and 11(b') we show the results for FRET rate ($1/\tau_{\text{FRT}}$) from QD to the mANT (circles) and $\gamma_{\text{FRT}}^{\text{nor}}$ during the fast (solid lines) and slow (dashed lines) processes. Here since we considered $R = 10$ nm, for y pol $1/\tau_{\text{FRT}}$ is rather very large. For x pol, however, $1/\tau_{\text{FRT}}$ is very small [Fig. 11(b')]. This is expected because of the wavelength of the plasmon peak for x pol is far from the QD transition (Fig. 8). $\gamma_{\text{FRT}}^{\text{nor}}$, however, follows the trend of population decay of the excitons. This rate reaches to $1/\tau_{\text{FRT}}$ when the value of δ becomes very small.

To study how the strength of the QD-induced exciton-plasmon coupling varies with R , in Fig. 12(a) we show the results for ρ_{21} when $R = 15$ (as in the experiments) and 150 nm for y pol. The results show that for $R = 15$ nm we can still see some signature of $\text{Re}[\rho_{21}]$. Under these conditions the $1/\tau_{\text{FRT}}$ is about 56 ns^{-1} (circles) while $\gamma_{\text{FRT}}^{\text{nor}}$ drops to about 42 ns^{-1} in the presence of the laser pulse. At $R = 150$ nm $\text{Re}[\rho_{21}]$ becomes nearly zero [Fig. 12(a)], while its $\text{Im}[\rho_{21}]$ remains similar to that of $R = 15$ nm (dashed lines). Figure 10(b) shows for $R = 150$ nm $1/\tau_{\text{FRT}}$ becomes insignificant (triangles).

VII. CONCLUSIONS

We investigate exciton-plasmon coupling and emission enhancement of QDs in functional metal-oxide plasmonic metastructures consisting of an array of gold mANTS embedded in Si and coated with an ultrathin layer of Al oxide. Our results showed that such metastructures can enhance emission of QDs well beyond what normal plamsonic effects can offer while elongating their lifetimes. We demonstrate the prime impact of localized surface-plasmon resonances in mANTS is making lifetime elongation more efficient and enhancing exciton-plasmon coupling. These results can underline the unique impact of efficient hot electron transfer from mANTS to the Si layer in the presence of Si/Al oxide charge barrier, leading to significant suppression of the defect environments of the QDs. Such a process allows QDs to set up efficient exciton-plasmon coupling, polarizing their spontaneous emission.

ACKNOWLEDGMENTS

This work is supported by U.S. National Science Foundation under Grant No. CMMI 1234823. R.G. and J.Z.W. acknowledge support by ARO Contract No. W911NF-16-1-0029, and NSF Contracts No. NSF-DMR-1337737 and No. NSF-DMR-1508494.

- [1] Maogang Gong, Qingfeng Liu, Brent Cook, Bhupal Kattel, Ti Wang, Wai-Lun Chan, Dan Ewing, Matthew Casper, Alex Stramel, and Judy Z. Wu, All-printable ZnO quantum dots/graphene van der Waals heterostructures for ultrasensitive detection of ultraviolet light, *ACS Nano* **11**, 4114 (2017).
- [2] E. Plum, V. A. Fedotov, P. Kuo, D. P. Tsai, and N. I. Zheludev, Towards the lasing spaser: Controlling metamaterial optical response with semiconductor quantum dots, *Opt. Express* **17**, 8548 (2009).
- [3] X. Brokmann, G. Messin, P. Desbiolles, E. Giacobino, M. Dahan, and J. P. Hermier, Colloidal CdSe/ZnS quantum dots as single-photon sources, *New J. Phys.* **6**, 99 (2004).
- [4] Mengxin Ren, Mo Chen, Wei Wu, Lihui Zhang, Junku Liu, Biao Pi, Xinzheng Zhang, Qunqing Li, Shoushan Fan, and Jingjun Xu, Linearly polarized light emission from quantum dots with plasmonic nanoantenna arrays, *Nano Lett.* **15**, 2951 (2015).
- [5] Kenji Tanaka, Eric Plum, Jun Yu Ou, Takashi Uchino, and Nikolay I. Zheludev, Multifold Enhancement of Quantum Dot Luminescence in Plasmonic Metamaterials, *Phys. Rev. Lett.* **105**, 227403 (2010).
- [6] Marcus Jones, Shun S. Lo, and Gregory D. Scholes, Quantitative modeling of the role of surface traps in CdSe/CdS/ZnS nanocrystal photoluminescence decay dynamics, *Proc. Natl. Acad. Sci.* **106**, 3011 (2009).
- [7] Yoichi Kobayashi, Takatoshi Nishimura, Hiroshi Yamaguchi, and Naoto Tamai, Effect of surface defects on

- Auger recombination in colloidal CdS quantum dots, *J. Phys. Chem. Lett.* **2**, 1051 (2011).
- [8] Huidong Zang, Hongbo Li, Nikolay S. Makarov, Kirill A. Velizhanin, Kaifeng Wu, Young-Shin Park, and Victor I. Klimov, Thick-shell CuInS₂/ZnS quantum dots with suppressed ‘blinking’ and narrow single-particle emission line widths, *Nano Lett.* **17**, 1787 (2017).
- [9] Alexander O. Govorov, Garnett W. Bryant, Wei Zhang, Timur Skeini, Jaebeom Lee, Nicholas A. Kotov, Joseph M. Slocik, and Rajesh R. Naik, Exciton-plasmon interaction and hybrid excitons in semiconductor-metal nanoparticle assemblies, *Nano Lett.* **6**, 984 (2006).
- [10] K. Lance Kelly, Eduardo Coronado, Lin Lin Zhao, and George C. Schatz, The optical properties of metal nanoparticles: The influence of size, shape, and dielectric environment, *J. Phys. Chem. B* **107**, 668 (2003).
- [11] M. Futamata, Y. Maruyama, and M. Ishikawa, Local electric field and scattering cross section of Ag nanoparticles under surface plasmon resonance by finite difference time domain method, *J. Phys. Chem. B* **107**, 7607 (2003).
- [12] Encai Hao and George C. Schatz, Electromagnetic fields around silver nanoparticles and dimers, *J. Chem. Phys.* **120**, 357 (2004).
- [13] Dentcho A. Genov, Andrey K. Sarychev, Vladimir M. Shalaev, and Alexander Wei, Resonant field enhancements from metal nanoparticle arrays, *Nano Lett.* **4**, 153 (2004).
- [14] Jörg P. Kottmann, Olivier J. F. Martin, David R. Smith, and Sheldon Schultz, Plasmon resonances of silver nanowires with a nonregular cross section, *Phys. Rev. B* **64**, 235402 (2001).
- [15] Daniel Ratchford, Farbod Shafei, Suenne Kim, Stephen K. Gray, and Xiaoqin Li, Manipulating coupling between a single semiconductor quantum dot and single gold nanoparticle, *Nano Lett.* **11**, 1049 (2011).
- [16] Anika Kinkhabwala, Zongfu Yu, Shanhui Fan, Yuri Avlasevich, Klaus Müllen, and W. E. Moerner, Large single-molecule fluorescence enhancements produced by a bowtie nanoantenna, *Nat. Photonics* **3**, 654 (2009).
- [17] Esteban Bermúdez Ureña, Mark P. Kreuzer, Stella Itzhakov, Hervé Rigneault, Romain Quidant, Dan Oron, and Jérôme Wenger, Excitation enhancement of a quantum dot coupled to a plasmonic antenna, *Adv. Mater.* **24**, OP314 (2012).
- [18] C. T. Yuan, Y. C. Wang, H. W. Cheng, H. S. Wang, M. Y. Kuo, M. H. Shih, and J. Tang, Modification of fluorescence properties in single colloidal quantum dots by coupling to plasmonic gap modes, *J. Phys. Chem. C* **117**, 12762 (2013).
- [19] Kasey J. Russell, Tsung-Li Liu, Shanying Cui, and Evelyn L. Hu, Large spontaneous emission enhancement in plasmonic nanocavities, *Nat. Photonics* **6**, 459 (2012).
- [20] Thang B. Hoang, Gleb M. Akselrod, Christos Argyropoulos, Jian Huang, David R. Smith, and Maiken H. Mikkelsen, Ultrafast spontaneous emission source using plasmonic nanoantennas, *Nat. Commun.* **6**, 7788 (2015).
- [21] B. Hoex, S. B. S. Heil, E. Langereis, M. C. M. van de Sanden, and W. M. M. Kessels, Ultralow surface recombination of *c*-Si substrates passivated by plasma-assisted atomic layer deposited Al₂O₃, *Appl. Phys. Lett.* **89**, 042112 (2006).
- [22] Scott K. Cushing, Jiangtian Li, Joeseph Bright, Brandon T. Yost, Peng Zheng, Alan D. Bristow, and Nianqiang Wu, Controlling plasmon-induced resonance energy transfer and hot electron injection processes in Metal@TiO₂Core–shell nanoparticles, *J. Phys. Chem. C* **119**, 16239 (2015).
- [23] Scott K. Cushing and Nianqiang Wu, Progress and perspectives of plasmon-enhanced solar energy conversion, *J. Phys. Chem. Lett.* **7**, 666 (2016).
- [24] Alexander O. Govorov, Hui Zhang, and Yurii K. Gunko, Theory of photoinduction of hot plasmonic carriers from metal nanostructures into semiconductors and surface molecules, *J. Phys. Chem. C* **117**, 16616 (2013).
- [25] Nikos Iliopoulos, Andreas F. Terzis, Vassilios Yannopoulos, and Emmanuel Paspalakis, Two-qubit correlations via a periodic plasmonic nanostructure, *Ann. Phys.* **365**, 38 (2016).
- [26] Vassilios Yannopoulos and Emmanuel Paspalakis, Giant enhancement of dipole-forbidden transitions via lattices of plasmonic nanoparticles, *J. Mod. Opt.* **62**, 1435 (2015).
- [27] Emmanuel Paspalakis, Sofia Evangelou, and Andreas F. Terzis, Control of excitonic population inversion in a coupled semiconductor quantum dot–metal nanoparticle system, *Phys. Rev. B* **87**, 235302 (2013).
- [28] Wen-Xing Yang, Ai-Xi Chen, Ziwen Huang, and Ray-Kuang Lee, Ultrafast optical switching in quantum dot–metallic nanoparticle hybrid systems, *Opt. Express* **23**, 13032 (2015).
- [29] S. M. Sadeghi, W. J. Wing, and R. R. Gutha, Undamped ultrafast pulsation of plasmonic fields via coherent exciton-plasmon coupling, *Nanotechnology* **26**, 085202 (2015).
- [30] Ali Hatef, S. M. Sadeghi, and Mahi R. Singh, Coherent molecular resonances in quantum dot–metallic nanoparticle systems: Coherent self-renormalization and structural effects, *Nanotechnology* **23**, 205203 (2012).
- [31] Seyed M. Sadeghi, Waylin J. Wing, Rithvik R. Gutha, and Christina Sharp, Semiconductor quantum dot super-emitters: Spontaneous emission enhancement combined with suppression of defect environment using metal-oxide plasmonic metafilms, *Nanotechnology* **29**, 015402 (2018).
- [32] Seyed M. Sadeghi, Waylin J. Wing, Rithvik R. Gutha, Jamie S. Wilt, and Judy Z. Wu, Balancing silicon/aluminum oxide junction for super-plasmonic emission enhancement of quantum dots via plasmonic metafilms, *Nanoscale* **10**, 4825 (2018).
- [33] Gregory V. Hartland, Optical studies of dynamics in noble metal nanostructures, *Chem. Rev.* **111**, 3858 (2011).
- [34] Christophe Voisin, Natalia Del Fatti, Dimitris Christofilos, and Fabrice Vallée, Ultrafast electron dynamics and optical nonlinearities in metal nanoparticles, *J. Phys. Chem. B* **105**, 2264 (2001).
- [35] H. Baida, Denis Mongin, D. Christofilos, Guillaume Bachelier, Aurélien Crut, Paolo Maioli, Natalia Del Fatti, and Fabrice Vallée, Ultrafast Nonlinear Optical Response of a Single Gold Nanorod Near its Surface Plasmon Resonance, *Phys. Rev. Lett.* **107**, 057402 (2011).
- [36] J. J. H. Gielis, Bram Hoex, M. C. M. Van de Sanden, and W. M. M. Kessels, Negative charge and charging dynamics in Al₂O₃ films on Si characterized by second-harmonic generation, *J. Appl. Phys.* **104**, 073701 (2008).
- [37] Bram Hoex, J. J. H. Gielis, M. C. M. Van de Sanden, and W. M. M. Kessels, On the *c*-Si surface passivation mechanism

- by the negative-charge-dielectric Al₂O₃, *J. Appl. Phys.* **104**, 113703 (2008).
- [38] K Patty, S. M. Sadeghi, A. Nejat, and C.-B. Mao, Enhancement of emission efficiency of colloidal CdSe quantum dots on silicon substrate via an ultra-thin layer of aluminum oxide, *Nanotechnology* **25**, 155701 (2014).
- [39] Kira Patty, Seyed M. Sadeghi, Quinn Campbell, Nathan Hamilton, Robert G. West, and Chuanbin Mao, Probing the structural dependency of photoinduced properties of colloidal quantum dots using metal-oxide photo-active substrates, *J. Appl. Phys.* **116**, 114301 (2014).
- [40] S. M. Sadeghi, W. J. Wing, R. R. Gutha, and L. Capps, Control of spontaneous emission of quantum dots using correlated effects of metal oxides and dielectric materials, *Nanotechnology* **28**, 095701 (2017).
- [41] Waylin J. Wing, Seyed M. Sadeghi, Rithvik R. Gutha, Quinn Campbell, and Chuanbin Mao, Metallic nanoparticle shape and size effects on aluminum oxide-induced enhancement of exciton-plasmon coupling and quantum dot emission, *J. Appl. Phys.* **118**, 124302 (2015).
- [42] Waylin J. Wing, Seyed M. Sadeghi, and Quinn Campbell, Improvement of plasmonic enhancement of quantum dot emission via an intermediate silicon-aluminum oxide interface, *Appl. Phys. Lett.* **106**, 013105 (2015).
- [43] Hans Mertens, Julie S. Biteen, Harry A. Atwater, and Albert Polman, Polarization-selective plasmon-enhanced silicon quantum-dot luminescence, *Nano Lett.* **6**, 2622 (2006).
- [44] G. Allan, C. Delerue, and M. Lannoo, Electronic Structure of Amorphous Silicon Nanoclusters, *Phys. Rev. Lett.* **78**, 3161 (1997).
- [45] Seyed M. Sadeghi, Rithvik R. Gutha, and Waylin J. Wing, Turning on plasmonic lattice modes in metallic nanoantenna arrays via silicon thin films, *Opt. Lett.* **41**, 3367 (2016).
- [46] Said Rahimzadeh Kalaleh Rodriguez, Aimi Abass, Björn Maes, Olaf T. A. , Janssen, and J., Gómez Rivas, Coupling Bright and Dark Plasmonic Lattice Resonances, *Phys. Rev. X* **1**, 021019 (2011).
- [47] Alan Vitrey, Lionel Aigouy, Patricia Prieto, José Miguel Garcá-Martí, and Mará U. González, Parallel collective resonances in arrays of gold nanorods, *Nanoletters* **14**, 2079 (2014).
- [48] Rithvik R. Gutha, Seyed M. Sadeghi, Christina Sharp, and Waylin J. Wing, Biological sensing using hybridization phase of plasmonic resonances with photonic lattice modes in arrays of gold nanoantennas, *Nanotechnology* **28**, 355504 (2017).
- [49] Joachim R. Krenn, Gerburg Schider, W. Rechberger, B. Lamprecht, Alfred Leitner, Franz R. Ausseregg, and J. C. Weeber, Design of multipolar plasmon excitations in silver nanoparticles, *Appl. Phys. Lett.* **77**, 3379 (2000).
- [50] Boris N. Khlebtsov and Nikolai G. Khlebtsov, Multipole plasmons in metal nanorods: Scaling properties and dependence on particle size, shape, orientation, and dielectric environment, *J. Phys. Chem. C* **111**, 11516 (2007).
- [51] Emma Kathryn Payne, Kevin L. Shuford, Sungho Park, George C. Schatz, and Chad A. Mirkin, Multipole plasmon resonances in gold nanorods, *J. Phys. Chem. B* **110**, 2150 (2006).
- [52] Koichi Okamoto, Saurabh Vyawahare, and Axel Scherer, Surface-plasmon enhanced bright emission from CdSe quantum-dot nanocrystals, *JOSA B* **23**, 1674 (2006).
- [53] Koshin Hosoki, Takeshi Tayagaki, Shinpei Yamamoto, Kazunari Matsuda, and Yoshihiko Kanemitsu, Direct and Stepwise Energy Transfer from Excitons to Plasmons in Close-packed Metal and Semiconductor Nanoparticle Monolayer Films, *Phys. Rev. Lett.* **100**, 207404 (2008).
- [54] W. Z. Lee, G. W. Shu, J. S. Wang, J. L. Shen, C. A. Lin, W. H. Chang, R. C. Ruaan, W. C. Chou, C. H. Lu, and Y. C. Lee, Recombination dynamics of luminescence in colloidalcdse/zns quantum dots, *Nanotechnology* **16**, 1517 (2005).
- [55] Gia-Wei Shu, Wan-Zhen Lee, I.-J. Shu, Ji-Lin Shen, James Cheng-An Lin, Walter H. Chang, Ruoh-Chyu Ruaan, and Wu Ching Chou, Photoluminescence of colloidal CdSe/ZnS quantum dots under oxygen atmosphere, *IEEE Trans. Nanotechnol.* **4**, 632 (2005).
- [56] Artjay Javier, Donny Magana, Travis Jennings, and Geofrey F. Strouse, Nanosecond exciton recombination dynamics in colloidal CdSe quantum dots under ambient conditions, *Appl. Phys. Lett.* **83**, 1423 (2003).
- [57] Sedat Nizamoglu and Hilmi V Demir, Resonant nonradiative energy transfer in CdSe/ZnS core/shell nanocrystal solids enhances hybrid white light emitting diodes, *Opt. Express* **16**, 13961 (2008).
- [58] Xiaoyong Wang, Lianhua Qu, Jiayu Zhang, Xiaogang Peng, and Min Xiao, Surface-related emission in highly luminescent CdSe quantum dots, *Nano Lett.* **3**, 1103 (2003).
- [59] V.I. Klimov, D.W. McBranch, C.A. Leatherdale, and M.G. Bawendi, Electron and hole relaxation pathways in semiconductor quantum dots, *Phys. Rev. B* **60**, 13740 (1999).
- [60] Sergio Brovelli, Richard D. Schaller, S. A. Crooker, Florencio Garcá-Santamará, Yongfen Chen, Ranjani Viswanatha, Jennifer A. Hollingsworth, Han Htoon, and Victor I. Klimov, Nano-engineered electron–hole exchange interaction controls exciton dynamics in core–shell semiconductor nanocrystals, *Nat. Commun.* **2**, 280 (2011).
- [61] Rithvik R. Gutha, Seyed M. Sadeghi, Ali Hatef, Christina Sharp, and Yongbin Lin, Ultrahigh refractive index sensitivity via lattice-induced meta-dipole modes in flat metallic nanoantenna arrays, *Appl. Phys. Lett.* **112**, 223102 (2018).
- [62] Tu Hong, Bhim Chamlagain, Shuren Hu, Sharon M. Weiss, Zhixian Zhou, and Ya Qiong Xu, Plasmonic hot electron induced photocurrent response at MoS₂–metal junctions, *ACS Nano* **9**, 5357 (2015).
- [63] Mark W. Knight, Yumin Wang, Alexander S. Urban, Ali Sobhani, Bob Y. Zheng, Peter Nordlander, and Naomi J. Halas, Embedding plasmonic nanostructure diodes enhances hot electron emission, *Nano Lett.* **13**, 1687 (2013).
- [64] S. M. Sadeghi, Ultrafast plasmonic field oscillations and optics of molecular resonances caused by coherent exciton-plasmon coupling, *Phys. Rev. A* **88**, 013831 (2013).
- [65] Anders Moelbjerg, Per Kaer, Michael Lorke, and Jesper Mørk, Resonance Fluorescence from Semiconductor

- Quantum Dots: Beyond the Mollow Triplet, *Phys. Rev. Lett.* **108**, 017401 (2012).
- [66] S.M. Sadeghi, Quantum coherence effects in hybrid nanoparticle molecules in the presence of ultra-short dephasing times, *Appl. Phys. Lett.* **101**, 213102 (2012).
- [67] Seyed M. Sadeghi and Chuanbin Mao, Quantum sensing using coherent control of near-field polarization of quantum dot-metallic nanoparticle molecules, *J. Appl. Phys.* **121**, 014309 (2017).
- [68] Alexander O. Govorov, Wei Zhang, Timur Skeini, Hugh Richardson, Jaebeom Lee, and Nicholas A. Kotov, Gold nanoparticle ensembles as heaters and actuators: Melting and collective plasmon resonances, *Nanoscale Res. Lett.* **1**, 84 (2006).